European Journal of Remote Sensing - 2016, 49: 137-156
doi: 10.5721/EuJRS20164908
Received 16/09/2015 accepted 07/03/2016

European Journal of Remote Sensing
An official journal of the Italian Society of Remote Sensing
www.aitjournal.com

A fast operative method for NDVI uncertainty estimation and its role in vegetation analysis

Enrico Borgogno-Mondino[1]*, Andrea Lessio[1] and Mario Angelo Gomarasca[2]

[1]Department of Agricultural, Forest and Food Sciences, Università di Torino, Largo Braccini 2, 10095, Grugliasco (TO), Italy
[2]National Research Council of Italy, Institute for Electromagnetic Sensing of the Environment (IREA), Via Bassini 15, 20133 Milano, Italy
*Corresponding author, e-mail address: enrico.borgogno@unito.it

Abstract
Vegetation indices represent an effective and widely used tool for monitoring vegetation changes in time and space. Unfortunately, in many works index uncertainty is not reported, making interpretation unreliable. In this paper we propose an operational approach for estimating NDVI uncertainty, based on the propagation of variance of factors defining the adopted radiative transfer model. Two Landsat 8 Operational Land Imager (OLI) images were used to test the method and discuss results. An agriculture-devoted area located in NW Italy was chosen as case study. Results showed that: a) the major contribution to NDVI uncertainty comes from topographic and atmospheric factors; b) uncertainty varies in space and time and depends on sensor spectral bands; c) NDVI uncertainty estimates can be exploited to map NDVI significant differences in space and time.
Keywords: Sensitivity analysis, NDVI accuracy, image calibration, Landsat 8OLI, radiative transfer model.

Introduction
In the context of optical remote sensing spectral indices represent a powerful tool to monitor and describe surfaces' changes in time and space with the goal of improving land management [Gilabert et al., 2002; Kallel et al., 2007; Jiang et al., 2008]. Specifically, vegetation indices are widely used in both forest and agriculture context, especially when large areas have to be monitored [Xiao and Moody, 2005]. Vegetation index products have been extensively used by the scientific community in vegetation [Azzali and Menenti, 2000] and biodiversity [Oindo and Skidmore, 2002] mapping, ecosystem phenology assessing [Schwartz et al., 2002] and becoming regularly used by natural resource managers and decision makers [Van Leeuwen and Orr, 2006].
A sensitivity analysis concerning primary data processing is very important for a correct interpretation of derived indices. In particular in change detection and multi-temporal analysis [Du et al., 2002; Janzen et al., 2006], this is a very important issue since significant index

differences has to be recognized. A quantification of the potential uncertainty of final products (e.g. of NDVI maps) is, therefore, essential. Primary data uncertainty, in fact, affects and impacts reliability of vegetation indices and related biophysical parameters [Huemmrich and Goward, 1992; Price, 1992], compromising their effectiveness. Nevertheless, works involving spectral indexes do not generally quantify uncertainty. This fact can be partially explained by the nature of the index itself, for which, in the most of cases, no reference data exists for a-posteriori validation that can be achieved only comparing some image-derived sample estimations with the correspondent ground surveyed ones [Beck et al., 2007; Verger et al., 2009]. Unfortunately, this step requires that a ground survey is made contemporarily to the flight by expensive spectro-radiometers and time consuming campaigns. These conditions cannot be satisfied for many applications and, for sure, when past acquisitions have to be processed. Where this situation occurs, the only possibility is to proceed to an a-priori (potential) uncertainty estimation of the final product that, necessarily, relies on a preventive estimation of uncertainty affecting reflectances used for index calculation, which are mainly related to the radiative transfer model (RTM) used to calibrate raw data. Literature is not so exhaustive concerning this issue. Attention is mainly focused on limits of sensors [Roderick et al., 1996; Li and Liu, 2012] and, when a trial is done, only one by one uncertainty responsible factor is considered. Many works, for example, reported that the impact of atmospheric scattering is not negligible [Miura et al., 2000; Tan et al., 2012, Vaudour et al., 2014], and that ortho-projection [Fontana et al., 2009] and topography [Hantson and Chuvieco, 2011; Singh et al., 2011] are impactful factors in at-the-ground reflectance recovering as well. Some other studies investigated the role of atmospheric scattering in determining uncertainty of indirect measures (e.g. LAI) through the adoption of physically based RTM [Myneni et al., 1997; Kobayashi et al., 2013; Mannschatz et al., 2014]. Nagol et al. [2009] tried to quantify NDVI uncertainty finding that it ranges between 0.03 and 0.08 for AVHRR data.

Huete [1994] stressed that "NDVI is unstable, varying with soil, sun-view geometry, atmospheric conditions, and the presence of dead material, as well as with changes within the canopy itself" but did not offer a quantification of these effects. Finally Burgess et al. [1995], referring to AVHRR data, underlined that "successful NDVI studies are carried out in large, relatively flat parts of the world (…). This type of terrain is ideal, given that the resolution of the data at nadir is relatively low at 1.1 km, and a large flat test site with contiguous ground cover allows statistically significant measurements to be made. However, the consequence of this is that the issue of the effect of topography on the NDVI measure has largely been ignored in the literature. If there is a dependence on topography, then there are many terrestrial areas where it is not reasonable to ignore the effect".

No specific work can, anyway, be found concerning a comprehensive study of uncertainty affecting index calculation. Therefore, an operational approach for its estimation is required, and, possibly, it should take into consideration those factors, as radiance, topography, transmittance, scattering and sun irradiance, that participates to the adopted RTM. The main goal of this work is the presentation of an operative approach for an a-priori estimation of at-the-ground reflectance (σ_ρ), NDVI and NDVI difference (in time) uncertainty (hereinafter called respectively σ_{NDVI} and $\sigma_{\Delta_{NDVI}}$). Since NDVI is probably the most widely used spectral index [Kerr and Ostrovsky, 2003; Pettorelli et al., 2005; Glenn et al., 2008], it was chosen as the representative of a wider group of remote sensing derived spectral indices. Consequently, presented methodology can be applied to all similar computations

concerning other indices. For their task authors applied the Variance Propagation Law (VPL) [Bevington and Robinson, 2002] to the simplified RTM described by Moran et al. [1992] to estimate σ_ρ and, successively, σ_{NDVI} and $\sigma_{\Delta_{NDVI}}$.
The test area, located in South Piedmont, North-Western Italy, represents a typical regional agricultural context surrounded by hilly and pre-mountainous zones.
Two Landsat 8 Operational Land Imager (OLI) [U.S. Geological Survey, 2015] acquisitions (September and October 2014) were used to investigate at-the-ground reflectance uncertainty and its effects along NDVI/NDVI difference computation, focusing on its distribution in space and time. Both images were therefore calibrated, into at-the-ground reflectance, using the above mentioned RTM and σ_ρ was contemporarily estimated for all bands. Moreover the contribution given by each factor involved in RTM to σ_ρ was investigated. Successively, NDVI and NDVI difference (October minus September) images were generated and the correspondent uncertainty estimated.

Test area

A circular test site of about 2,000 km² (Fig. 1) having a radius of 25 km and centered on UTM 32 WGS84 coordinates 394248 E, 4947222 N was selected. This part of Italy (Piedmont Region, NW Italy) is typically characterized by a continental climate. Alpine reliefs separate this area from the Mediterranean Sea, thus determining different local climatic conditions, with special regard on temperature trends, sun radiation and wind. The area is flat and the Langhe hill system characterizes its eastern part, while Alps limit the south western part. Agricultural and livestock activities are the major economic activities in the area (Fig. 2). Forests are marginal and, mainly, located in mountainous areas. Landscape is highly fragmented. Main patches are maize crops, fruit orchards and vineyards. The above mentioned land use statistics were derived from the Land-use/Land-cover map (LULC) available for this study (see "Available Data").

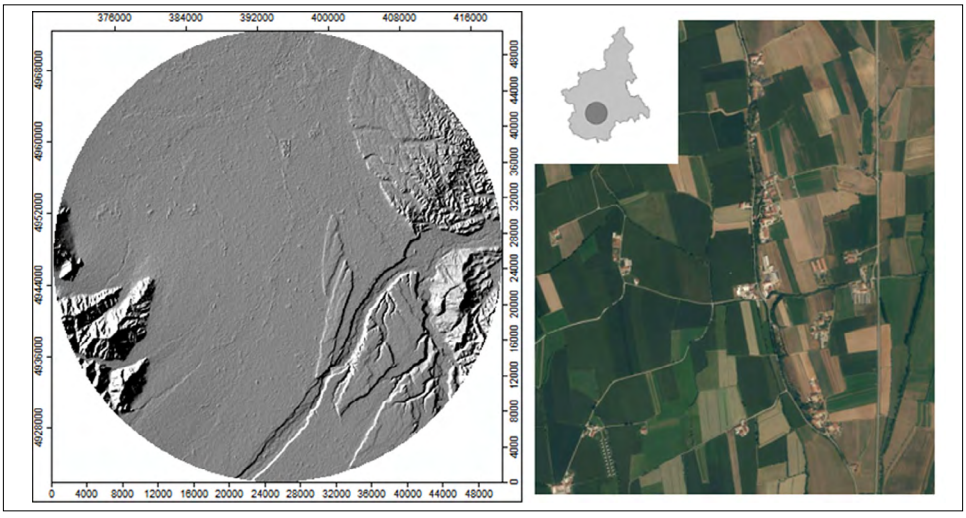

Figure 1 - (Left) Hillshade map of the test area calculated on DEM obtained from the Piedmont Region cartographic office. (Upper center) Area location within Piedmont Region (NW Italy). (Right) Typical agricultural landscape patterns of the area (from Google Earth).

Langhe hill system has recently been included in the UNESCO heritage (whc.unesco.org/en/list/). This kind of landscape is quite challenging for OLI sensor since its geometric resolution (30 m) is not exactly proper for the mean size of local patches (about 3 ha), determining a huge number of mixed pixels.
The choice of processing an image subset including hilly and mountainous areas was mandatory to emphasize the effect of terrain topography over final σ_ρ and σ_{NDVI}.

Land Cover classes	Percentage
Urban	5.78 %
Arable	61.16 %
Forest	12.16 %
Orchard, Vineyard	9.15 %
Plain meadows	6.31 %
Other classes	5.45 %

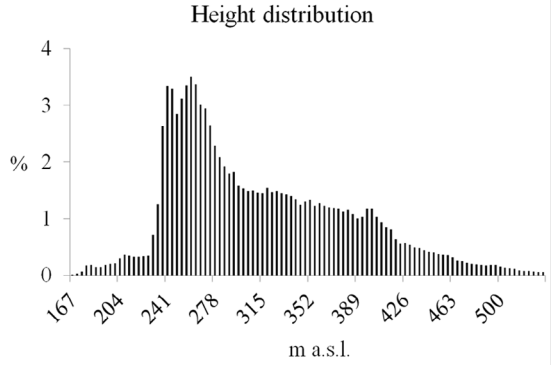

Figure 2 - Test area characteristics: (left) area percentages of main land use classes (IPLA S.p.A.). (Right) height classes distribution (m above sea level) calculated on DEM obtained from the Piedmont Region cartographic office.

Available Data

Two OLI Landsat 8 Level 1 data products were obtained for free from EarthExplorer distribution system [earthexplorer.usgs.gov]. Technical features of images are reported in Table 1.

Table 1 - Metadata of Landsat 8 OLI images used in this work.

	September 12th, 2014	October 23rd, 2014
Scene ID	LC81950292014255LGN00	LC81940292014296LGN00
Date	12/09/2014	23/10/2014
Time	10:17:27.0911536	10:11:20.9752253
Sun elevation angle	46.77204921	32.54716480
Sun azimuth	153.55852655	162.72172168
Path	195	194
Row	29	29

Landsat 8 OLI sensor has a mean geometrical resolution of 30 meters for visible-infrared bands (bands 1-7, 9), 15 meters for the panchromatic one (band 8) and 100 meters for the thermal ones (bands 10-11). Panchromatic (PAN, 0.50 - 0.68 μm), cirrus (1.36 - 1.38 μm)

and thermal bands (TIRS1, 10.60 - 11.19 µm; TIRS2, 11.50 - 12.51 µm) were not considered for this study. Radiometric resolution is 12-bits (rescaled to 16-bits when processed into Level-1 data products) [U.S. Geological Survey, 2015].
DEM (Digital Elevation Model) required by RTM to accomplish image topographic correction was freely obtained from the Piedmont Region cartographic office (http://www.geoportale.piemonte.it/geocatalogorp/?sezione=catalogo). The original geometrical resolution is 50 m, height accuracy is 2.5 m [Borgogno-Mondino et al., 2004] and the reference system is WGS84 UTM 32N. For this work, the original data was oversampled to 30 m resolution and aligned to L8 OLI images. Moreover, with the aim of minimizing local anomalies, responsible of some artifacts in the calibrated images, the DEM was filtered (low pass, 3x3 kernel). We assumed that these operations did not change DEM height accuracy.
The available LULC vector map (1:25000 scale) was used to explore if and how cover type conditions $\sigma_{\Delta_{NDVI}}$. LULC was freely available from the online database of the Piedmont Region (http://www.geoportale.piemonte.it/geocatalogorp/?sezione=catalogo) and supplied in the WGS84 UTM 32N reference system. Produced by IPLA (Institute for trees, wood, and environment S.p.A.) and co-founded by European Union, LULC is aimed at supporting studies for the territorial forest planning.

Methods

For a great number of applications there is no possibility to obtain low cost validations concerning index maps (e.g. NDVI) they are based on. Traditional validation in fact relies on the comparison between a reference dataset and estimations given by a model. This approach is also called "a-posteriori" variance estimation. The critical point is that, to obtain a reference dataset (test set) concerning NDVI (or simply at-the-ground reflectance) a ground survey has to be done. And, even if for ongoing acquisition this is possible (but expensive), for those applications relying on archive images and past datasets this cannot be done anymore. The only alternative is to focus on potential uncertainty that could affect the final product. This is referred to as "a-priori" variance [Brinker and Minnick, 1995]. The approach that ordinary statistics provides to face the problem is the VPL. It permits to estimate the effect of variance (ordinarily assumed as indicator of precision) of direct measurements (radiance, terrain topography, atmospheric scattering, atmospheric transmission, sun irradiance, etc.) over the one of indirect measurements (reflectances and indices) obtained by calculation. The starting point to successfully operate with VPL is to rigorously define the model formula it has to be applied to. While discussing about spectral indices and their application in a change detection context, the problem can be faced proceeding along three sequential steps. Firstly, we have to describe how uncertainty of factors participating to the image calibration model (i.e. the RTM) affects at-the-ground reflectance variance. Successively, at-the-ground reflectance variance has to be propagated along index calculation. Finally, if two NDVI images of different dates have to be compared by differencing, a further variance propagation must be taken into account; local index difference variance depends, in fact, on index variance at the two dates in that position. The local estimation of index difference uncertainty permits to separate significant from not-significant index variations (in time). The entire workflow chart is reported in Figure 3.

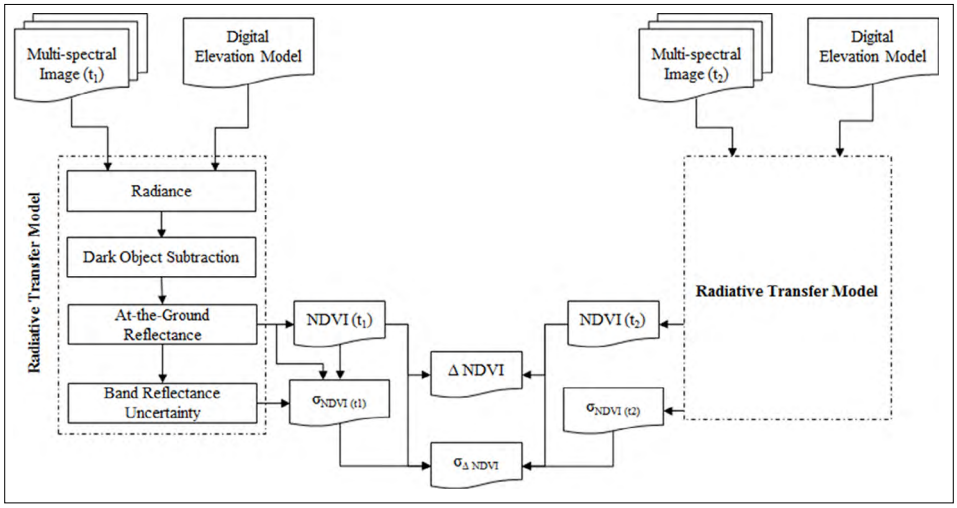

Figure 3 - Workflow for NDVI uncertainty estimation by Variance Propagation Law.

Pre-processing

An open approach (fully controllable and accessible by user) for image calibration is mandatory to control variance propagation. Therefore, image calibration and atmospheric correction was achieved by the simplified RTM by Moran et al. [1992], based on a dark object subtraction (DOS) approach [Chavez, 1996]. According to Moran RTM at-the-ground reflectance (ρ_λ) is given by Equation [1].

$$\rho_\lambda(x,y) = \frac{\pi \cdot d^2 \cdot \left[L_\lambda(x,y) - \hat{L}_\lambda^{atm} \right]}{\tau_\lambda \cdot \left[\tau_\lambda \cdot sin\left[\beta(x,y) \right] \cdot I_\lambda + E_{down} \right]} \quad [1]$$

where ρ_λ is the at-the-ground reflectance value, L_λ is the at-sensor-radiance [$W \cdot sr^{-1} \cdot m^{-2} \cdot \mu m^{-1}$] obtained by applying gain and offset values supplied with L8 OLI images, $\hat{L}_\lambda^{atm}$ is the upwelling atmospheric scattered radiance [$W \cdot sr^{-1} \cdot m^{-2} \cdot \mu m^{-1}$], d the Sun-Earth distance coefficient (astronomical units), E_{down} the scattered downwelling contribution (that we assumed equal to $\pi \cdot \hat{L}_\lambda^{atm}$), τ_λ the atmospheric transmittance, β the sun incidence angle (rad) calculated at each position (pixel) using a DEM and I_λ the sun irradiance [$W \cdot m^{-2} \cdot \mu m^{-1}$] calculated according to Equation [2] from (http://semiautomaticclassificationmanual.readthedocs.org/en/latest/Landsat_conversion.html).

$$I_\lambda = \pi \cdot \frac{L_{max}^\lambda}{\rho_{max}^\lambda} \quad [2]$$

where L_{max}^λ is the band maximum radiance value and ρ_{max}^λ the correspondent maximum

reflectance value. Both values were obtained from L8 OLI datasets metadata file (MTL). Sun incidence angle map was generated by Analytical Hillshading tool of SAGA GIS 2.1.4 [Tarini et al., 2006] from the available DEM. For this work τ_λ was considered constant over the scene, equal for both images and just band dependent (Tab. 2). It was given for a reference summertime mid-latitude low-hazy atmosphere (20 km visibility) according to Fenn et al. [1985].

Table 2 - Atmospheric transmittance values given for a reference summertime mid-latitude low-hazy atmosphere.

L8 OLI band n.	Atmospheric transmittance
1	0.50
2	0.60
3	0.65
4	0.65
5	0.80
6	0.89
7	0.92

During these operations the contribution given by each RTM factor to reflectance uncertainty (σ_ρ) was estimated together with σ_ρ (see section "Pre-processing inputs and σ_ρ estimation").

RTM sensitivity analysis: variance propagation law

VPL (Eq. [3]) is a statistical sensitivity analysis technique that generates estimates of a-priori variance for a statistical variable (y) depending on some other independent ones (x_i).

$$\sigma_y^2 = \left(\frac{\partial y}{\partial x_1}\right)^2_{\overline{x_1}} \cdot \sigma_{x_1}^2 + \left(\frac{\partial y}{\partial x_2}\right)^2_{\overline{x_2}} \cdot \sigma_{x_2}^2 + \ldots + \left(\frac{\partial y}{\partial x_n}\right)^2_{\overline{x_n}} \cdot \sigma_{x_n}^2 \qquad [3]$$

where $y = f(x_1, x_2, \ldots, x_n)$ is the dependent variable, x_i the independent ones and $\sigma^2_{x_i}$ their variance (supposed to be known). It is worth to remind that standard deviation (squared root of variance) of errors can be interpreted as precision of a measure. VPL requires that partial derivatives of ρ respect to each RTM factor (independent variables) are calculated at each position (pixel), confirming that reflectance variance is natively space dependent. According to Equation [1] VPL applied to RTM can be written as:

$$\sigma_{\rho_\lambda} = \sqrt{\left(\frac{\partial \rho}{\partial L}\right)^2_{L_\lambda} \cdot \sigma^2_{L_\lambda} + \left(\frac{\partial \rho}{\partial \hat{L}^{atm}}\right)^2_{\hat{L}_\lambda^{atm}} \cdot \sigma^2_{\hat{L}_\lambda^{atm}} + \left(\frac{\partial \rho}{\partial \beta}\right)^2_{\beta} \cdot \sigma^2_{\beta} + \left(\frac{\partial \rho}{\partial \tau}\right)^2_{\tau_\lambda} \cdot \sigma^2_{\tau} + \left(\frac{\partial \rho}{\partial I}\right)^2_{I_\lambda} \cdot \sigma^2_{I}} \qquad [4]$$

VPL was applied to Equation [1] under the following hypotheses:

a) all independent variables are not correlated to each other;
b) five independent variables conditioning uncertainty of at-the-ground reflectance are considered: $L_\lambda(x,y), \hat{L}_\lambda^{atm}\ \tau_\lambda, \beta(x,y), I_\lambda$.

Once VPL is formalized, the variance of involved RTM factors must be known, supposed or somehow derived.

Pre-processing inputs and σ_ρ estimation

RTM and VPL analysis require that some inputs are supplied. Some of them can be deduced from imagery metadata (e.g. sun elevation and azimuth angles, image *gain* and *offset* value, sun irradiance, image radiometric resolution) or from auxiliary data (sun incidence angle image, DEM and DEM height accuracy). Some others are strictly dependent on model itself that has in charge their estimation (e.g. σ_β). Some are constant, others band dependent, space dependent or both. In Table 3 authors have summarized specifications of factors' variances involved in VPL analysis.

Table 3 - Formulas used to estimate standard deviation of factors involved in VPL analysis.

Factor		Definition	Description
At-sensor-Radiance [W·sr^{-1}·m^{-2}·µm^{-1}]	$L_\lambda(x,y)$	$\sigma_{L_\lambda} = \frac{\text{GAIN}_\lambda \cdot (2^{16}-1)}{(2^{12}-1)}$	Constant over the scene, different for each band. It is assumed to be equal to the original (12 bits) radiometric resolution of L8 OLI imagery.
Atmospheric scattering [W·sr^{-1}·m^{-2}·µm^{-1}]	$\hat{L}_\lambda^{atm}$	$\sigma_{\hat{L}_\lambda}^{atm} = 0.05 \cdot \hat{L}_\lambda^{atm}$	Different for each band, constant over the scene.
Atmospheric transmittance	τ_λ	$\sigma_{\tau_\lambda} = 0.05 * \tau_\lambda$	Different for each band, constant over the scene
Sun Irradiance [W·m^{-2}·µm^{-1}]	I_λ	σ_{I_λ}	Equal for all bands and constant over the scene.
Sun incidence angle [rad]	$\beta(x,y)$	$\sigma_\beta = \frac{\sqrt{2}\cdot\sigma_{\text{DEM}}}{2\text{GSD}\cdot\left[1+\left(\frac{\Delta h(x,y)}{\text{GSD}}\right)^2\right]}$	Equal for all bands, varying over the scene. Δh is the maximum local height difference around the pixel calculated from DEM (cell size = GSD).

Standard deviation values of Table 3, once propagated by VPL, contribute differently to final reflectance variance. We measured and mapped the relative weight (importance) of each RTM factor variance (σ_i^2) on reflectance variance σ_ρ (Tab. 4). Since RTM factor variance weight is local (different at each position), in Table 8 we reported the mean value of weights for each band. We separated *vegetated* from *not-vegetated* pixels by thresholding

NDVI images at 0.5. We appositely used this value to ensures that vegetated pixels were sufficiently pure. In fact in literature NDVI values under 0.5 are generally related to partially vegetated pixels [Momeni and Saradjian, 2006].

Table 4 - Contribution given by variance (σ^2) of each RTM factor to the total reflectance variance.

Radiance	Atmospheric scattering	Sun incidence angle	Atmospheric transmittance	Sun irradiance
$\frac{\left(\frac{\partial \rho}{\partial L}\right)^2 \cdot \sigma^2_{L_\lambda}}{\sigma^2_{\rho_\lambda}(x,y)}$	$\frac{\left(\frac{\partial \rho}{\partial L}\right)^2 \cdot \sigma^{atm}_{\hat{L}_\lambda}}{\sigma^2_{\rho_\lambda}(x,y)}$	$\frac{\left(\frac{\partial \rho}{\partial \beta}\right)^2 \cdot \sigma^2_{\beta}(x,y)}{\sigma^2_{\rho_\lambda}(x,y)}$	$\frac{\left(\frac{\partial \rho}{\partial \tau}\right)^2 \cdot \sigma^2_{\tau}(x,y)}{\sigma^2_{\rho_\lambda}(x,y)}$	$\frac{\left(\frac{\partial \rho}{\partial I}\right)^2 \cdot \sigma^2_{I}}{\sigma^2_{\rho_\lambda}(x,y)}$

NDVI and NDVI difference variance estimation

NDVI and NDVI difference uncertainty were finally estimated. As far as NDVI is concerned the formula is the canonic one given by Rouse et al. [1974] [5]:

$$NDVI(x,y) = \frac{\rho_{NIR}(x,y) - \rho_{RED}(x,y)}{\rho_{NIR}(x,y) + \rho_{RED}(x,y)} \quad [5]$$

where $\rho_{NIR}(x,y)$ and $\rho_{RED}(x,y)$ are respectively the at-the-ground reflectance in the NIR and RED bands (5 and 4 for L8 OLI images). Partial derivatives were calculated assuming that $\rho_{NIR}(x,y)$ and $\rho_{RED}(x,y)$ are uncorrelated and independent statistical variables. $\sigma_{NDVI}(x,y)$ estimation is given by Equation [6].

$$\sigma_{NDVI}(x,y) = \sqrt{\left(\frac{2 \cdot \rho_{RED}(x,y)}{\left[\rho_{RED}(x,y) + \rho_{NIR}(x,y)\right]^2}\right)^2 \cdot \sigma^2_{\rho NIR}(x,y) + \left(-\frac{2 \cdot \rho_{NIR}(x,y)}{\left[\rho_{NIR}(x,y) + \rho_{RED}(x,y)\right]^2}\right)^2 \cdot \sigma^2_{\rho RED}(x,y)} \quad [6]$$

$\sigma^2_{\rho NIR}(x,y)$ and $\sigma^2_{\rho RED}(x,y)$ were obtained at the previous step. They represent local variance of reflectance in RED and NIR bands.

Successively NDVI difference, $\Delta_{NDVI}(x,y)$, was computed by Equation [7] and its uncertainty, $\sigma_{\Delta NDVI}(x,y)$, estimated by Equation [8]. Finally significant NDVI differences were mapped and statistically summarized using two different thresholds (1σ and 2σ), using Equation [9]. Statistics are given for main LULC classes.

$$\Delta_{NDVI}(x,y) = NDVI_{Oct}(x,y) - NDVI_{Sept}(x,y) \quad [7]$$

$$\sigma_{\Delta NDVI}(x,y) = \sqrt{\sigma_{NDVI}(x,y)_{Oct}^{\ 2} + \sigma_{NDVI}(x,y)_{Sept}^{\ 2}} \quad [8]$$

$$SD(x,y) = \left|\Delta_{NDVI}(x,y)\right| > \sigma_{\Delta_{NDVI}}(x,y) \quad [9]$$

Image pre-processing, VPL analysis and σ_{NDVI} and $\sigma_{\Delta_{NDVI}}$ estimation were implemented by the research group in the IDL (Interactive Data Language, ITT Visual Information Solutions) 8.0.1 programming language.

Results and discussion

VPL inputs and σ_{ρ} estimation

At-the-sensor-radiance images were obtained applying *gain* and *offset* values contained in metadata provided with L8 OLI images (Tab. 5).

Table 5 - Gain and offset as reported in the metadata files of images used for this study.

L8 OLI band n.	September 12th, 2014		October 23rd, 2014	
	Gain	*Offset*	*Gain*	*Offset*
1	0.012396	-61.97885	0.012683	-63.41270
2	0.012693	-63.46710	0.012987	-64.93538
3	0.011697	-58.48439	0.011967	-59.83740
4	0.009864	-49.31733	0.010092	-50.45827
5	0.006036	-30.17975	0.006176	-30.87794
6	0.001501	-7.50543	0.001536	-7.67906
7	0.000506	-2.52973	0.000518	-2.58826

Sun irradiances were calculated using Equation [2]. Radiance maximum, reflectance maximum and Earth-Sun distance coefficents (d) were obtained from image metadata. Values are reported in Table 6.

Table 6 - Sun irradiance values and metadata parameters used for its calculation.

L8 OLI band n.	Wavelength [µm]	Sun Irradiance [W·m^{-2}·µm^{-1}]	Max Radiance (Sept) [W·sr^{-1}·m^{-2}·µm^{-1}]	Max Radiance (Oct) [W·sr^{-1}·m^{-2}·µm^{-1}]	L8 OLI Max reflectance
1	0.435–0.451	1972.2530	750.3780	767.7376	1.2107
2	0.452–0.512	2019.6110	768.3962	786.1727	1.2107
3	0.533–0.590	1861.0550	708.0705	724.4514	1.2107
4	0.636–0.673	1569.3460	597.0850	610.8983	1.2107
5	0.851–0.879	960.3620	365.3862	373.8393	1.2107
6	1.566–1.651	238.8330	90.8682	92.9704	1.2107
7	2.107–2.294	80.5000	30.6274	31.3360	1.2107
d_{Sept} = 1.0064325			d_{Oct} = 0.9949890		

Atmospheric scattered radiance was estimated for each band based on DOS approach, while transmittance was assumed constant over the scene and different for each band (see Tab. 2). During radiometric calibration reflectance variance was estimated too by VPL analysis. Standard deviation values supplied or calculated for all factors are reported in Table 7.

Table 7 - Standard deviation values of factors involved in VPL analysis. For those depending on position, only minimum and maximum value are reported.

September 12th, 2014		**b1**	**b2**	**b3**	**b4**	**b5**	**b6**	**b7**
At-sensor radiance [$W{\cdot}sr^{-1}{\cdot}m^{-2}{\cdot}\mu m^{-1}$]		0.1984	0.2031	0.1872	0.1579	0.0966	0.0240	0.0081
Atmospheric scattering $\left(\sigma_{\hat{L}_\lambda}^{atm} = 0.05 \cdot \hat{L}_\lambda^{atm}\right)$ [$W{\cdot}sr^{-1}{\cdot}m^{-2}{\cdot}\mu m^{-1}$]		0.7935	0.8125	0.4279	0.6314	0.2247	0.0555	0.0186
Atmospheric transmittance $\left(\sigma_{\tau_\lambda} = 0.05 \cdot \tau_\lambda\right)$		0.025	0.030	0.033	0.033	0.040	0.045	0.046
Sun irradiance [$W{\cdot}m^{-2}{\cdot}\mu m^{-1}$]		0.0500 fixed (user instrument/source dependent)						
Sun incidence angle [rad] (grid)	*(max)*	0.0589 fixed (DEM dependent)						
	(min)	0.0319 fixed (DEM dependent)						
October 23rd, 2014		**b1**	**b2**	**b3**	**b4**	**b5**	**b6**	**b7**
At-sensor radiance [$W{\cdot}sr^{-1}{\cdot}m^{-2}{\cdot}\mu m^{-1}$]		0.2030	0.2078	0.1915	0.1615	0.0988	0.0246	0.0083
Atmospheric scattering [$W{\cdot}sr^{-1}{\cdot}m^{-2}{\cdot}\mu m^{-1}$]		0.3169	0.0954	0.2386	0.6460	0.2242	0.0572	0.0129
Atmospheric transmittance		0.025	0.030	0.033	0.033	0.040	0.045	0.046
Sun Irradiance [$W{\cdot}m^{-2}{\cdot}\mu m^{-1}$]		0.0500 fixed (instrument dependent)						
Sun incidence angle [rad] (grid)	*(max)*	0.0589 fixed (DEM dependent)						
	(min)	0.0319 fixed (DEM dependent)						

During tests standard deviation of sun irradiance was set to 0.05 $W.m^{-2}.\mu m^{-1}$, while σ_{τ_λ} and $\sigma_{\hat{L}_\lambda}^{atm}$ were assumed equal to the 5% of the correspondent τ_λ and $\hat{L}_\lambda^{atm}$ values.
Many tests performed by varying σ_I in the range [0.05-10.00] demonstrated that no significant contribution is given by this term to reflectance variance; in fact maximum difference recorded for $\sigma_{\rho\lambda}$ was about 0.0001. Sun incidence angle variance (Tab. 3) was calculated according to the available DEM having a cell size of 30 m and σ_{DEM} = 2.5 m. The same values were considered along all computations. Table 8 shows that, averagely, topography is the most influencing factor of reflectance uncertainty, due to its heavy impact over sun incidence angle calculation. This is the dominant source of error for infrared bands, while for the visible ones significant contribution also comes from atmospheric scattering $\left(\sigma_{\hat{L}_\lambda}^{atm}\right)$ and radiance $\left(\sigma_{L_\lambda}\right)$ factors. For band 1 the prevailing factor is scattering for vegetated areas, while sun incidence angle effect prevails in not-vegetated ones. Transmittance and sun irradiance appear to be always negligible.

Table 8. Contribution given by each factor to reflectance variance. Values are expressed in percentage and statistics are given separately for permanently vegetated areas (at the two dates) and for not-vegetated ones. (**) are maximum values, (*) is other significant contributions.

Mean class value		*Factor*	*b1*	*b2*	*b3*	*b4*	*b5*	*b6*	*b7*
Sept	Vegetated	At-sensor radiance	3.78	2.36	1.66	1.72	0.072	0.34	1.31
		Scattering	64.24**	41.33*	9.75*	30.22*	0.64	2.24	7.83*
		Sun incidence angle	29.85*	53.54**	87.40**	65.84**	98.21**	96.40**	89.74**
		Transmittance	2.13	2.77	1.18	2.22	1.08	1.02	1.11
		Sun Irradiance	~ 0.00	~ 0.00	~ 0.00	~ 0.00	~ 0.00	~ 0.00	0.01
	Not Vegetated	At-sensor radiance	2.15	1.20	0.81	0.56	0.16	0.34	0.63
		Scattering	37.97*	22.07*	5.00	10.66*	1.21	2.17	3.82
		Sun incidence angle	55.90**	72.97**	92.95**	85.92**	97.58**	96.48**	94.39**
		Transmittance	3.99	3.76	1.24	2.87	1.05	1.00	1.15
		Sun Irradiance	~ 0.00	~ 0.00	~ 0.00	~ 0.00	~ 0.00	~ 0.00	0.01
Oct	Vegetated	At-sensor radiance	24.74*	21.28*	3.04	2.05	0.05	0.14	0.54
		Scattering	60.85**	4.60	5.08*	35.09*	0.44	1.04	1.56
		Sun incidence angle	14.34*	74.10**	91.73**	62.00**	99.10**	98.41**	97.69**
		Transmittance	0.06	0.02	0.15	0.86	0.41	0.41	0.20
		Sun Irradiance	~ 0.00	~ 0.00	~ 0.00	~ 0.00	~ 0.00	~ 0.00	0.01
	Not Vegetated	At-sensor radiance	7.47*	3.26	0.95	0.45	0.13	0.11	0.19
		Scattering	19.11*	0.74	1.69	8.63*	0.91	0.84	0.59
		Sun incidence angle	73.10**	95.96**	97.20**	89.68**	98.56**	98.65**	99.01**
		Transmittance	0.32	0.03	0.16	1.23	0.40	0.40	0.21
		Sun Irradiance	~ 0.00	~ 0.00	~ 0.00	~ 0.00	~ 0.00	~ 0.00	0.01

In spite of these general considerations, weights are however varying over the scene, determining specific local relative influences that, sometimes, can be surprisingly different from the average behavior.

Relative weights of factors' variance are useful to understand which of them mainly contributes to degrade the quality of reflectance calculations; nevertheless they do not inform about the amount of final potential error affecting at-the-ground reflectance. For this

purpose we calculated for each L8 OLI band the median value (over the scene) of $\sigma_{\rho\lambda}$ and reported it in the graphs of Figure 4 for both considered dates.

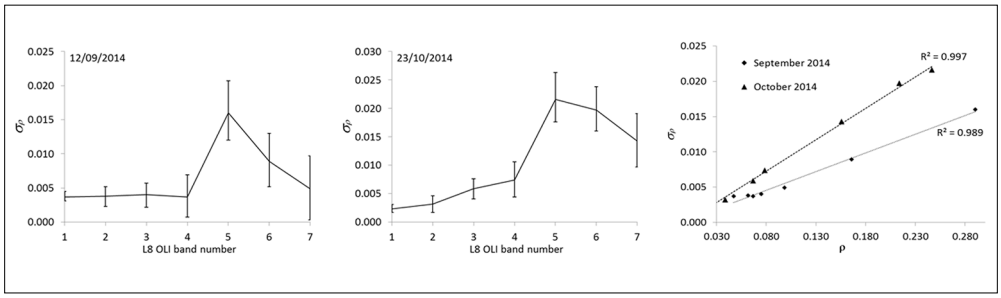

Figure 4 - $\sigma_{\rho\lambda}$ (scene median value) versus L8 OLI bands for September (left) and October (centre) image; trends are consistent with spectrum of the prevalent class in image (vegetation in September, bare soil in October). Error bars refer to 1st and 4th quartiles. (Right image) Linear regression relating reflectance and its standard deviation (median values) for each band.

Trends of Figure 4 (right) clearly shows how $\sigma_{\rho\lambda}$ strictly depends linearly on reflectance. This determines that reflectance uncertainty profile well correlates with spectral signature demonstrating that local variance depends on surface type. A further demonstration comes from left and central images of Figure 4, where $\sigma_{\rho\lambda}$ trends are similar to the ones expected for the spectrum of the prevailing class (in terms of m^2) over image: vegetation in September, bare soil in October (when maize crops have been harvested). Furthermore it can be observed that distribution of $\sigma_{\rho\lambda}$ around its median value is quite symmetric and generally increases while signal increases. Moreover $\sigma_{\rho\lambda}$ appears to change with season. In fact when sun is lower over the horizon (about 32° in October and about 47° in September) $\sigma_{\rho\lambda}$ is higher (right image of Fig. 4) demonstrating, once more, the importance of sun incidence angle in determining reliable ρ_λ measurement.

Successively, we focused on the relationship between *NDVI (x,y)* and $\sigma_{NDVI}(x,y)$ images, finding that a strong correlation exists (Fig. 5). Particularly, the higher is NDVI value, the lower is its uncertainty. It can also be noticed that the majority of pixels in September are vegetated (highest frequencies are in the NDVI range [0.6-0.9]), while in October they are not vegetated anymore (highest frequencies are in the NDVI range [0.2-0.4]). This depends on maize crop harvest that took place in the transitional period. Where highest frequencies occur the Noise-to-Signal ratio $(\sigma_{NDVI} / NDVI)$ is about 0.210 in October and 0.027 in September that is almost 10 times less. It means that scientific applications adopting NDVI as indicator of something different from vegetation, or for vegetation studies in extreme situations where plants are sparse or weakly active, have to carefully consider uncertainty to get their final conclusions. On the contrary, focusing on areas with active vegetation (NDVI = 0.7-0.9), almost the same uncertainty value (about 0.02) is maintained independently from other conditions, suggesting that strength of signal minimizes effects of any contribution to index variance.

In terms of absolute value of σ_{NDVI} it can be noticed that it reaches the highest values

(about 0.07) in October, when degradation effects of sun elevation angle over reflectance (and consequently over NDVI) are stronger. In September values are lower (up to 0.045) even for not vegetated pixels (lowest values of NDVI).

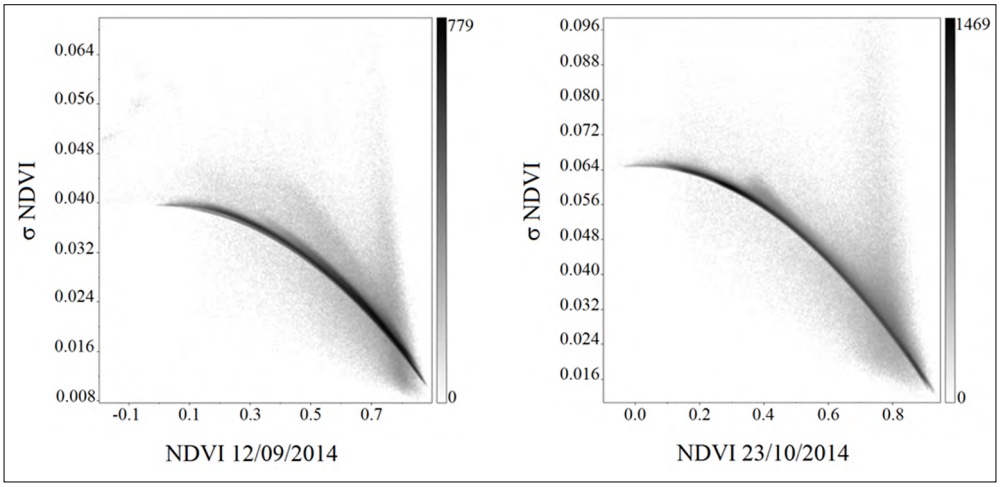

Figure 5 - Scatterplot relating NDVI and NDVI uncertainty (σ_{NDVI}) in September and October 2014. Right sided grayscale bar reports frequency (number of pixels).

Successively, we computed NDVI difference image $(\Delta_{NDVI}(x,y))$, October minus September 2014 (Fig. 6 - left). Correspondent uncertainty, $\sigma_{\Delta_{NDVI}}(x,y)$ image (Fig. 6 - right), was also calculated applying VPL to the difference formula ([7] and [8]). A correlation analysis was performed to investigate relationship between $\sigma_{\Delta_{NDVI}}(x,y)$ and $\Delta_{NDVI}(x,y)$. No correlation was found. In Figure 6 (lower right) it can be noticed that $\sigma_{\Delta_{NDVI}}$ values are not negligible at all, since about 50 % of pixels present a NDVI difference uncertainty in the range [0.06 - 0.08]. If compared with the range of variability of NDVI difference itself (Fig. 6 – lower left) it can be summarized that, averagely, the noise of measure is about 15% of signal.

In order to stress practical effects of such approach we, finally, used the previously generated information to map significant and not-significant NDVI changes occurred in the observation period in the study area. We assumed that $\sigma_{\Delta_{NDVI}}$ represented the sensibility for appreciating local index changes. NDVI difference values lower than an arbitrary multiple (generally 1 or 2) of the local $\sigma_{\Delta_{NDVI}}(x,y)$ were labeled as not-significant, stating that, at that position, nothing really changed. Results are given for both $1\sigma_{\Delta NDVI}$ and $2\sigma_{\Delta NDVI}$ considering different LULC classes (Tab. 9), to emphasize once more, that surface type conditions accuracy of NDVI measurement.

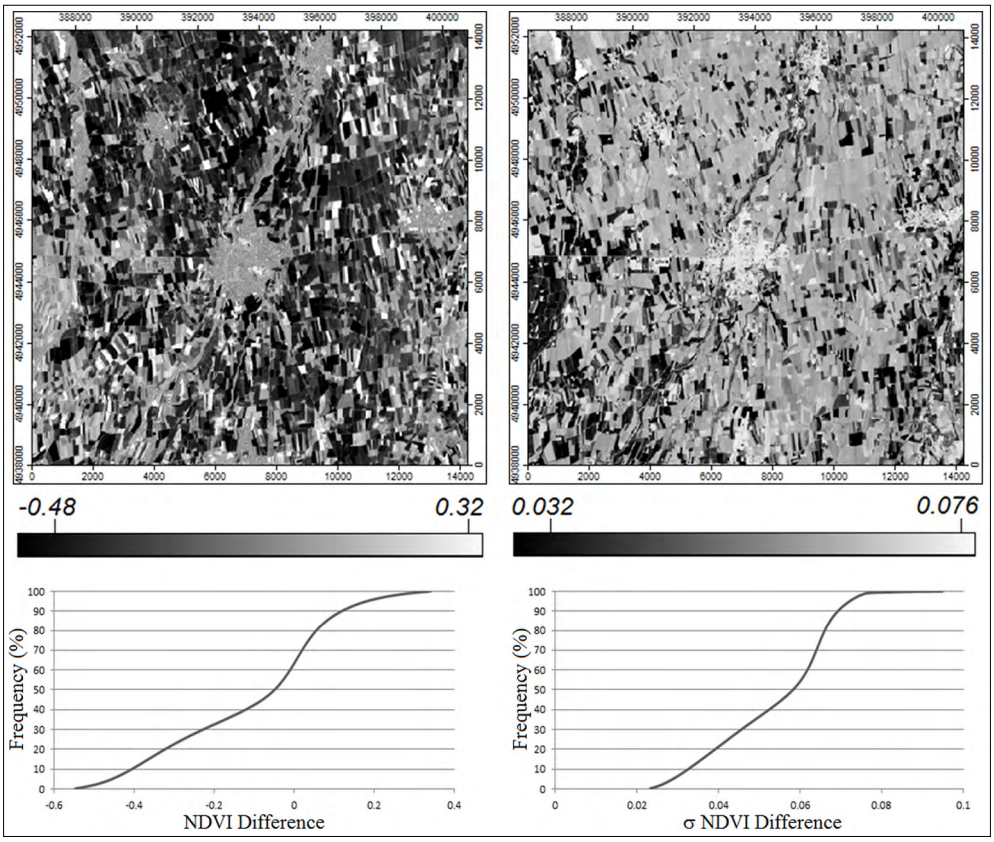

Figure 6 - (Upper left): a sample subset of $\Delta_{NDVI}(x,y)$. (Lower left): cumulative frequency function of $\Delta_{NDVI}(x,y)$ for the whole area. (Upper right): sample subset of $\sigma_{\Delta_{NDVI}}(x,y)$. (Lower right): cumulative frequency function of $\sigma_{\Delta_{NDVI}}(x,y)$ for the test area.

Table 9. Percentages of NDVI significant differences in the period October-September 2014 calculated for different LULC classes.

	$\sigma_{\Delta_{NDVI}}(x,y)$		$2\sigma_{\Delta_{NDVI}}(x,y)$	
	Significant [%]	**Not significant [%]**	**Significant [%]**	**Not significant [%]**
Urban	34.5	65.5	14.1	85.9
Arable	84.8	15.2	72.0	28.0
Orchard, Vineyard	66.4	33.6	42.4	57.6
Meadows	83.6	16.4	68.9	31.1
Forest	50.4	49.6	30.0	70.0
Other classes	43.6	56.4	19.3	80.7
Total	73.7	26.3	57.8	42.2

Table 9 shows that the total area significantly changed between September and October 2014, is about 74 % for $1\sigma_{\Delta NDVI}$ threshold and only about 58% for $2\sigma_{\Delta NDVI}$. Majority of changes are related to maize crops harvest that occurred in the reference period. Significant NDVI differences are, in fact, mostly located over harvested/agricultural areas where percentage of changes reaches 84.8% and 72.0% respectively for $1\sigma_{\Delta NDVI}$ and $2\sigma_{\Delta NDVI}$. Unchanged (or not-significantly changed) areas represent the 26.3% and 42.2% of the whole, respectively for 1 and $2\sigma_{\Delta NDVI}$ thresholds.

Urban and forested areas are the ones where unchanged pixels represent the highest percentage (between about 65% and 86 % for urban and between 50% and 70% for forest respectively for $1\sigma_{\Delta NDVI}$ and $2\sigma_{\Delta NDVI}$) confirming that our method correctly detect invariant surfaces. Significantly changed areas of these classes can be related to "mixed" pixels or to effectively changing small sized surfaces of other classes that were included in the polygons of the biggest one surrounding them in the LULC vector map, during classification simplification step.

Conclusions

In this work we focused on the importance of estimating uncertainty related to spectral measurements from L8 OLI images. We have proposed an operational "a-priori" approach that can be used in many applications related to spectral index calculation, able to easily estimate variance of at-the-ground calibrated reflectances and, consequently, of the index itself. The method relies on the Variance Propagation Law and requires that an "open" RTM is used during image calibration. For this study the simplified "open" RTM by Moran et al. [1992] was implemented in an IDL environment. The use of a completely accessible and controllable RTM allowed to investigate contribution of every considered physical factor to reflectance, NDVI and NDVI difference variance.

Results demonstrate that the most influencing factor for reflectance variance is sun incidence angle. Its effects over reflectance variance are strictly related to accuracy of DEM used for topographic correction. The higher is DEM accuracy, the lower is at-the-ground reflectance uncertainty. Therefore, since morphological factor proved to be decisive on final data quality, it cannot be neglected in computation, also when reflectances are aggregated for index calculation. It is commonly retained that the use of indexes built in shape of ratios can minimize or completely remove the "variable illumination effects in areas of topographic slope" [Mather, 2005]. In particular this conviction comes from a mathematical consideration concerning [1] where the sine factor that participates to reflectance computation can be mathematically simplified. This assumption is true just if the TOA (Top-of-Atmosphere) reflectance is calculated; on the contrary it is false if a more complete RTM is used. Specifically the additive scattering term in denominator of [1] excludes this possibility: topographic term has therefore to be considered and, consequently, it conditions $\sigma_{\rho\lambda}$. Among other factors just those related to atmospheric scattering and to at-the-sensor radiance contribute significantly to $\sigma_{\rho\lambda}$, especially for visible bands. In particular atmospheric scattering influence is comparable to the one of sun incidence angle for bands 1 and 2, especially for vegetated surfaces. Contribution of transmittance and sun irradiance variance to $\sigma_{\rho\lambda}$ is always negligible. Moreover we showed that is strongly correlated to at-the-ground reflectance and consequently that it depends on surface type and season (Fig. 4).

As far as NDVI and NDVI difference is concerned, we found that σ_{NDVI} strongly and inversely correlates with NDVI values (Fig. 5). No correlation instead was found between $\sigma_{\Delta_{NDVI}}$ and Δ_{NDVI} value. The values that our method estimated for σ_{NDVI} are consistent with the ones reported for other sensors [Nagol et al., 2009]. We also showed that σ_{NDVI} and $\sigma_{\Delta_{NDVI}}$ can be effectively used to better interpret data. Specifically, significant NDVI differences can be recognized and separated from the ones due to intrinsic uncertainty of recording instrument or RTM. The proposed case study confirmed this potentiality. In fact the highest percentage of significant NDVI changes occurring in the reference period were found for seasonally changing LULC classes (harvested areas); on the contrary the lowest percentage of NDVI changes were found for the expected unchanging classes (urban, bare soils, forest, water, etc.).
Authors retain that this approach can effectively be applied to all spectral indexes and sensors, helping to improve reliability of many results concerning change detection and spectral index mapping.

References

Azzali A., Menenti M. (2000) - *Mapping vegetation-soil complexes in southern Africa using temporal Fourier analysis of NOAA AVHRR NDVI data*. International Journal of Remote Sensing, 21: 973-996. doi: http://dx.doi.org/10.1080/014311600210380.

Beck P.S.A., Jönsson P., Høgda K.A., Karlsen S.R., Eklundh L., Skidmore A.K. (2007) - *A ground-validated NDVI dataset for monitoring vegetation dynamics and mapping phenology in Fennoscandia and the Kola peninsula*. International Journal of Remote Sensing, 28 (19): 4311-4330. doi: http://dx.doi.org/10.1080/01431160701241936.

Bevington P.R., Robinson D.K. (2002) - *Data reduction and error analysis for the physical sciences*. McGraw-Hill Science/Engineering/Math, 3rd Edition.

Borgogno-Mondino E., Giulio Tonolo F., Boccardo P., Bellone T. (2004) - *DTMs generation from satellite stereo images: accuracy tests in mountain region*. Proceedings of 11th SPIE - Remote Sensing for Environmental Monitoring, 5574: 341-350. doi: http://dx.doi.org/10.1117/12.565564.

Brinker R.C., Minnick R. (1995) - *The surveying handbook*. Springer-Verlag, 2nd Edition. doi: http://dx.doi.org/10.1007/978-1-4615-2067-2.

Burgess D.W., Lewis P., Mulled J.P. (1995) - *Topographic effects in AVHRR NDVI data*. Remote Sensing of Environment, 54: 223-232. doi: http://dx.doi.org/10.1016/0034-4257(95)00155-7.

Chavez P.S. (1996) - *Image-based atmospheric corrections*. Revisited and Improved Photogrammetric Engineering and Remote Sensing, [Falls Church, Va.] American Society of Photogrammetry, 62: 1025-1036.

Du Y., Teillet P.M., Cihlar J. (2002) - *Radiometric normalization of multitemporal high-resolution satellite images with quality control for land cover change detection*. Remote Sensing of Environment, 82: 123-134. doi: http://dx.doi.org/10.1016/S0034-4257(02)00029-9.

Fenn R.W., Clough S.A., Gallery W.O., Good R.E., Kneizys F.X., Mill J.D., Rothman L.S., Shettle E.P., Voltz F.E. (1985) - *Handbook of geophysics and space environment*. Cap.18: Optical and infrared properties of the atmosphere. Air Force Cambridge

Research Laboratories (U.S.).

Fontana F.M.A., Trishchenko A.P., Khlopenkov A.P., Luo Y., Wunderle S. (2009) - *Impact of orthorectification and spatial sampling on maximum NDVI composite data in mountain regions*. Remote Sensing of Environment, 113: 2701-2712. doi: http://dx.doi.org/10.1016/j.rse.2009.08.008.

Gilabert M.A., Gonzalez-Piqueras J., Garcia-Haro F.J., Melia J. (2002) - *A generalized soil-adjusted vegetation index*. Remote Sensing of Environment, 82: 303-310. doi: http://dx.doi.org/10.1016/S0034-4257(02)00048-2.

Glenn E.P., Huete A.R., Nagler P.L., Nelson S.G. (2008) - *Relationship between remotely-sensed vegetation indices, canopy attributes, and plant physiological process: what vegetation indices can and cannot tell us about landscape*. Sensors, 8: 2136-2160. doi: http://dx.doi.org/10.3390/s8042136.

Hantson S., Chuvieco E. (2011) - *Evaluation of different topographic correction methods for Landsat imagery.* International Journal of Applied Earth Observation and Geoinformation, 13: 691-700. doi: http://dx.doi.org/10.1016/j.jag.2011.05.001.

Huemmrich K.F., Goward S.N. (1992) - *Spectral vegetation indexes and the remote sensing of biophysical parameters*. Proceedings of International Geoscience and Remote Sensing Symposium, Houston, 2: 1017-1019. doi: http://dx.doi.org/10.1109/IGARSS.1992.578329.

Huete A.R., Liu H.Q. (1994) - *An error and sensitivity analysis of the atmospheric- and soil-correcting variants of the NDVI for the MODIS-EOS*. IEEE Transactions on Geoscience and Remote Sensing, 32: 897-905. doi: http://dx.doi.org/10.1109/36.298018.

Janzen D.T., Fredeen A.L., Wheate R.D. (2006) - *Radiometric correction techniques and accuracy assessment for Landsat TM data in remote forested regions*. Canadian Journal of Remote Sensing, 32 (5): 330-334. doi: http://dx.doi.org/10.5589/m06-028.

Jiang Z., Huete A.R., Didan K., Miura T. (2008) - *Development of a two-band enhanced vegetation index without a blue band*. Remote Sensing of Environment, 112: 3833-3845. doi: http://dx.doi.org/10.1016/j.rse.2008.06.006.

Kallel A., Le-Hégarat-Mascle S., Ottlé C., Hubert-Moy L. (2007) - *Determination of vegetation cover fraction by inversion of a four parameter model based on isoline parametrization*. Remote Sensing of Environment, 111: 553-566. doi: http://dx.doi.org/10.1016/j.rse.2007.04.006.

Kerr J.T., Ostrovsky M. (2003) - *From space to species: ecological applications for remote sensing*. Trends in Ecology & Evolution, 18 (6): 299-305. doi: http://dx.doi.org/10.1016/S0169-5347(03)00071-5.

Kobayashi H., Ryu Y., Baldocchi D.D., Welles J.M., Norman J.M. (2013) - *On the correct estimation of gap fraction: how to remove scattered radiation in gap fraction measurements?* Agricultural and Forest Meteorology, 174-175 (2013): 170-183. doi: http://dx.doi.org/10.1016/j.agrformet.2013.02.013.

Li X.L., Liu R. (2012) - *Research on the assessment of HJ-1A NDVI accuracy*. Proceedings of 2012 International Conference on Measurement, Information and Control, MIC 2012, 1: 121-124.

Mannschatz T., Pflug B., Borg E., Feger K.H., Dietrich P. (2014) - *Uncertainties of LAI estimation from satellite imaging due to atmospheric correction*. Remote Sensing of Environment, 153: 24-39. doi: http://dx.doi.org/10.1016/j.rse.2014.07.020.

Mather P.M. (2005) - *Computer processing of remotely-sensed images: an introduction*. Third Edition, John Wiley & Sons, Incorporation, pp. 140-144.

Miura T., Huete A.R., Yoshioka H. (2000) - *Evaluation of sensor calibration uncertainties on vegetation indices for MODIS*. IEEE Transactions on Geoscience and Remote Sensing, 38: 1399-1409. doi: http://dx.doi.org/10.1109/36.843034.

Momeni M., Saradjian M.R. (2006) - *Evaluating NDVI-based emmissivities of MODIS bands 31 and 32 using emissivities derived by Day/Night LST algorithm*. Remote Sensing of Environmement, 106: 190-198. doi: http://dx.doi.org/10.1016/j.rse.2006.08.005.

Moran M., Jackson R., Slater P., Teillet P. (1992) - *Evaluation of simplified procedures for retrieval of land surface reflectance factors from satellite sensor output*. Remote Sensing of Environment, 41: 169-184. doi: http://dx.doi.org/10.1016/0034-4257(92)90076-V.

Myneni R.B., Nemani R.R., Running S.W. (1997) - *Estimation of global leaf area and absorbed PAR using radiative transfer models*. IEEE Transactions on Geoscience and Remote Sensing, 35: 1380-1393. doi: http://dx.doi.org/10.1109/36.649788.

Nagol J.R., Vermote E.F., Prince S.D. (2009) - *Effects of atmospheric variation on AVHRR NDVI data.* Remote Sensing of Environment, 113: 392-397. doi: http://dx.doi.org/10.1016/j.rse.2008.10.007.

Oindo B.O., Skidmore A.K. (2002) - *Interannual variability of NDVI and species richness in Kenya*. International Journal of Remote Sensing, 23: 285-298. doi: http://dx.doi.org/10.1080/01431160010014819.

Pettorelli N., Vik J.O., Mysterud A., Gaillard J.M., Tucker C.J., Stenseth N.C. (2005) - *Using the satellite-derived NDVI to assess ecological responses to environmental change*. Trends in Ecology & Evolution, 20 (9): 503-510. doi: http://dx.doi.org/10.1016/j.tree.2005.05.011.

Price J.C. (1992) - *Estimating vegetation amount from visible and near-infrared reflectances*. Remote Sensing of Environment, 41: 29-34. doi: http://dx.doi.org/10.1016/0034-4257(92)90058-R.

Roderick M., Smith R., Cridland S. (1996) - *The Precision of the NDVI derived from AVHRR observations*. Remote Sensing of Environment, 56: 57-65. doi: http://dx.doi.org/10.1016/0034-4257(95)00213-8.

Rouse J.W., Haas R.W., Schell J.A., Deering D.W., Harlan J.C. (1974) - *Monitoring the vernal advancement and retrogradation (greenwave effect) of natural vegetation*. NASA/GSFCT Type III Final Report, Greenbelt, MD, USA.

Schwartz M.D., Reed B.C., White M.A. (2002) - *Assessing satellite-derived start of season measures in the conterminous USA*. International Journal of Climatology, 22: 1793-1805. doi: http://dx.doi.org/10.1002/joc.819.

Singh S., Sharma J.K., Mishra V.D. (2011) - *Comparison of different topographic correction methods using AWiFS satellite data*. International Journal of Advanced Engineering Sciences and Technologies, 7: 103-109.

Tan K.C., Lim H.S., MatJafri M.Z., Abdullah K. (2012) - *A comparison of radiometric correction techniques in the evaluation of the relationship between LST and NDVI in Landsat imagery*. Environmental Monitoring and Assessment, 184: 3813-3829. doi: http://dx.doi.org/10.1007/s10661-011-2226-0.

Tarini M., Cignoni P., Montani C. (2006) - *Ambient occlusion and edge cueing to enhance real time molecular visualization*. IEEE Transactions on Visualization and Computer

Graphics, 12 (5): 1237-1244. doi: http://dx.doi.org/10.1109/TVCG.2006.115.

U.S. Geological Survey (2015) - *Landsat 8 (L8) Data Users Handbook*, U.S. Department of the Interior.

Van Leeuwen W.J.D., Orr B.J. (2006) - *Spectral vegetation indices and uncertainty: Insights from a user's perspective*. IEEE Transactions on Geoscience and Remote Sensing, 44: 1931-1933. doi: http://dx.doi.org/10.1109/TGRS.2006.873688.

Vaudour E., Gilliot J.M., Bel L., Bréchet L., Hamiache J., Hadjar D., Lemonnier Y. (2014) - *Uncertainty of soil reflectance retrieval from SPOT and RapidEye multispectral satellite images using a per-pixel bootstrapped empirical line atmospheric correction over an agricultural region*. International Journal of Applied Earth Observation and Geoinformation, 26: 217-234. doi: http://dx.doi.org/10.1016/j.jag.2013.07.003.

Verger A., Martínez B., Coca F.C.D., García-Haro F.J. (2009) - *Accuracy assessment of fraction of vegetation cover and leaf area index estimates from pragmatic methods in a cropland area*. International Journal of Remote Sensing, 30: 2685-2704. doi: http://dx.doi.org/10.1080/01431160802555804.

Xiao A.J., Moody A. (2005) - *A comparison of methods for estimating fractional green vegetation cover within a desert-to-upland transition zone in central New Mexico, USA*. Remote Sensing of Environment, 98: 237-250. doi: http://dx.doi.org/10.1016/j.rse.2005.07.011.